JOURNAL OF COMPUTATIONAL PHYSICS 97, 414–443 (1991)

High-Order Splitting Methods for the Incompressible Navier–Stokes Equations

GEORGE EM KARNIADAKIS

Mechanical and Aerospace Engineering, Princeton University, Princeton, New Jersey 08544

MOSHE ISRAELI

Department of Computer Science, Technion-Israel Institute of Technology, Haifa, Israel

AND

STEVEN A. ORSZAG

Program in Applied Mathematics, Princeton University, Princeton, New Jersey 08544

Received October 11, 1989; revised August 1, 1990

A new pressure formulation for splitting methods is developed that results in high-order time-accurate schemes for the solution of the incompressible Navier–Stokes equations. In particular, improved pressure boundary conditions of high order in time are introduced that minimize the effect of erroneous numerical boundary layers induced by splitting methods. A new family of stiffly stable schemes is employed in mixed explicit/implicit time-intgration rules. These schemes exhibit much broader stability regions as compared to Adams-family schemes, typically used in splitting methods. Their stability properties remain almost constant as the accuracy of the integration increases, so that robust third- or higher-order time-accurate schemes can readily be constructed that remain stable at relatively large CFL number. The new schemes are implemented within the framework of spectral element discretizations in space so that flexibility and accuracy is guaranteed in the numerical experimentation. A model Stokes problem is studied in detail, and several examples of Navier–Stokes solutions of flows in complex geometries are reported. Comparison is made with the previously used first-order in time spectral element splitting and non-splitting (e.g., Uzawa) schemes. High-order splitting/spectral element methods combine accuracy in space and time, and flexibility in geometry, and thus can be very efficient in direct simulations of turbulent flows in complex geometries.

1. INTRODUCTION

The numerical solution of the unsteady incompressible Navier–Stokes equations that govern viscous flows requires discretization in both space and time. Spatial

0021-9991/91 $3.00

discretization relates directly to resolution of the most important small-scale features of the flow (e.g., boundary layers, streaks, etc.) as well as the size of the problem. Temporal discretization, however, relates to unsteady flow phenomena (e.g., oscillations), but also dictates directly the form of system of the semi-discrete equations to be solved. In particular, the temporal discretization determines the form of the pressure equation and represents how well the incompressibility constraint is approximated in pressure–velocity formulations.

The pressure in incompressible flows plays a very particular role as it should always be in equilibrium with a time-dependent divergence-free velocity field, but it does not appear explicitly in the equation imposing such a divergence condition. While it is clear that the governing equation for pressure is a Poisson equation derived from the momentum equation by requiring incompressibility, it is less clear what boundary conditions (BC) the pressure should be subject to. In recent work Gresho and Sani [1] and Orszag *et al.* [2] addressed the issue of pressure BC and concluded that a Neumann-type BC derived from the normal to domain boundary momentum equation leads to a correct pressure solution. In particular, in [1] it was argued that in the absence of singularities as $t \to 0$ properly derived Neumann and Dirichlet BCs lead to the same solution; however, Neumann BCs are more general and always provide a unique solution for $t \geqslant 0$.

In splitting methods [3], which are the methods we analyze in this work, the pressure satisfies a Poisson equation with compatible Neumann BCs. The exact form of this BC is very important not only because it directly affects the overall accuracy of the scheme, but also because it determines the efficiency of the time-stepping algorithm. This is particularly true in simulations of unsteady flows in complex geometries, where a separately solvable second-order pressure equation is still the only affordable approach. Splitting methods in conjunction with spectral and spectral element methods have been used with success in simulating highly unsteady flows in nonperiodic and very complex geometries [4–6]. In these studies, splitting led to first-order accuracy, so that very small time steps were required in order to prevent significant time-differencing and splitting errors.

There have been a number of attempts in the last decade to modify the classical splitting method, so that high-order time accuracy be obtained [7–9]. A more systematic analysis was given more recently in [2], where various different approaches were suggested to circumvent the spurious effects of splitting errors without any significant loss in efficiency or ease in implementation. Our work here is inspired primarily by the work in [2, 10]; in both papers several boundary conditions for incompressible flows are analyzed and tested for a simple Stokes problem. Our objective is to implement an iproved splitting scheme within the context of spectral element discretizations [11–13]. The good resolution properties of spectral operators allow elimination of all spatial errors, so errors in the solutions reflect only time differencing errors or errors due to splitting of operators.

In Section 2, we review the splitting method and present the new, high-order pressure boundary conditions; the formulation is general and independent of the spatial discretization scheme. However, in order to achieve high spatial accuracy we

employ spectral element discretizations for all the tests presented. In Section 3 we study in detail a model Stokes problem that has been studied extensively previously both analytically and numerically [2, 10]. In Section 4 we introduce and analyze med stiffly stable schemes, and we finally present several test examples in Section 5.

2. Semi-Discrete Formulation

We consider here Newtonian, incompressible flows with constant properties, which are governed by the Navier–Stokes equations written in the form,

$$\frac{\partial \mathbf{v}}{\partial t} = -\nabla p + \nu \mathbf{L}(\mathbf{v}) + \mathbf{N}(\mathbf{v}) \qquad \text{in} \quad \Omega, \tag{1a}$$

subject to the incompressibility constraint

$$Q \equiv \nabla \cdot \mathbf{v} = 0 \qquad \text{in} \quad \Omega, \tag{1b}$$

where $\mathbf{v}(= u\hat{x} + v\hat{y} + w\hat{z})$ is the velocity vector, p is the static pressure, and ν is the kinematic viscosity. Here $\mathbf{L}$ and $\mathbf{N}$ repreent the linear and nonlinear operators, respectively, and are defined as

$$\mathbf{L}(\mathbf{v}) \equiv \nabla^2 \mathbf{v} = \nabla(\nabla \cdot \mathbf{v}) - \nabla \times (\nabla \times \mathbf{v}) \tag{1c}$$

$$\mathbf{N}(\mathbf{v}) \equiv -\tfrac{1}{2}[\mathbf{v} \cdot \nabla \mathbf{v} + \nabla(\mathbf{v} \cdot \mathbf{v})]. \tag{1d}$$

The nonlinear terms are written here in a skew-symmetric form following the suggestions in [14] in order to minimize aliasing effects. To proceed we would like to integrate (1a), using high-order time-stepping schemes; such schemes are routinely used for the numerical solution of ordinary differential equations, however their use in the present context gives rise to several questions: (1) derivation of mixed explicit–implicit schemes and appropriate treatment of the pressure term; (2) investigation of stability and accuracy properties of such mixed schemes. In the present section we set up the framework for the mixed Adams–Bashforth/Adams–Moulton family. Later, in Section 4 we will consider more general multistep families.

Upon integration of (1a) over one time step Δt we obtain

$$\mathbf{v}^{n+1} - \mathbf{v}^n = -\int_{t_n}^{t_{n+1}} \nabla p \, dt + \nu \int_{t_n}^{t_{n+1}} \mathbf{L}(\mathbf{v}) \, dt + \int_{t_n}^{t_{n+1}} \mathbf{N}(\mathbf{v}) \, dt, \tag{2a}$$

where the superscript index n refers to time level $t_n \equiv n \Delta t$. We can further rewrite the pressure term as

$$\int_{t_n}^{t_{n+1}} \nabla p \, dt = \Delta t \, \nabla \bar{p}^{n+1} \tag{2b}$$

so that $\bar{p}^{n+1}$ is the scalar field that ensures that the final velocity field is incompressible at the end of time level $(n+1)$. It has been common practice (for efficiency reasons) to approximate the nonlinear terms via an explicit scheme, for example, a J_e-order scheme from the Adams–Bashforth family as

$$\int_{t_n}^{t_{n+1}} \mathbf{N}(\mathbf{v})\, dt = \Delta t \sum_{q=0}^{J_e-1} \beta_q \mathbf{N}(\mathbf{v}^{n-q}), \tag{2c}$$

where β_q are appropriately chosen weights [15]. The linear terms are approximated via implicit schemes for stability reasons; such an approximation, using for example, a scheme of order J_i from the Adams–Moulton family gives

$$\int_{t_n}^{t_{n+1}} \mathbf{L}(\mathbf{v})\, dt = \Delta t \sum_{q=0}^{J_i-1} \gamma_q \mathbf{L}(\mathbf{v}^{n+1-q}), \tag{2d}$$

where γ_q are appropriately chosen weights for the implicit scheme [15]. The above system of Eq. (1), along with the incompressibility constraint, form a strongly coupled system.

Solution to this semi-discrete system of equations can be obtained by further splitting Eq. (2a) into three substeps as

$$\frac{\hat{\mathbf{v}} - \mathbf{v}^n}{\Delta t} = \sum_{q=0}^{J_e-1} \beta_q \mathbf{N}(\mathbf{v}^{n-q}) \qquad \text{in} \quad \Omega \tag{3a}$$

$$\frac{\hat{\hat{\mathbf{v}}} - \hat{\mathbf{v}}}{\Delta t} = -\nabla \bar{p}^{n+1} \qquad \text{in} \quad \Omega \tag{3b}$$

$$\frac{\mathbf{v}^{n+1} - \hat{\hat{\mathbf{v}}}}{\Delta t} = \nu \sum_{q=0}^{J_i-1} \gamma_q \mathbf{L}(\mathbf{v}^{n+1-q}) \qquad \text{in} \quad \Omega \tag{3c}$$

with Dirichlet boundary conditions $\vec{v}_0$

$$\mathbf{v}^{n+1} = \vec{v}_0 \qquad \text{on} \quad \partial\Omega. \tag{3d}$$

Here $\hat{\mathbf{v}}$, $\hat{\hat{\mathbf{v}}}$ are intermediate velocity fields defined in (3a)–(3b). The classical splitting method proceeds by introducing two further assumptions: first that the field $\hat{\hat{\mathbf{v}}}$ satisfies the incompressibility constraint, and thus

$$\nabla \cdot \hat{\hat{\mathbf{v}}} = 0 \qquad \text{in} \quad \Omega; \tag{4a}$$

and second that the same field $\hat{\hat{\mathbf{v}}}$ also satisfies the prescribed Dirichlet condition in the direction $\mathbf{n}$, normal to the boundary,

$$\hat{\hat{\mathbf{v}}} \cdot \mathbf{n} = \vec{v}_0 \cdot \mathbf{n}. \tag{4b}$$

Incorporating these assumptions into Eq. (3b) we finally arrive at a separately solvable elliptic equation for the pressure with Neumann boundary conditions in the form,

$$\nabla^2 \bar{p}^{n+1} = \nabla \cdot \left(\frac{\hat{\mathbf{v}}}{\Delta t} \right) \qquad \text{in} \quad \Omega \tag{4c}$$

$$\frac{\partial \bar{p}^{n+1}}{\partial n} = -\frac{\vec{v}_0 \cdot \mathbf{n} - \hat{\mathbf{v}} \cdot \mathbf{n}}{\Delta t} \qquad \text{on} \quad \partial\Omega. \tag{4d}$$

The final field $\mathbf{v}^{n+1}$ is then obtained by solving the Helmholtz equation (3c)–(3d) with the field $\hat{\mathbf{v}}$ acting as a forcing term.

The above splitting approach although very efficient in practice, produces solutions that often suffer from large splitting errors which may lead to erroneous results [7]. The reason for that is primarily the imposition of the incorrect boundary condition (4b), which is inconsistent with the continuous equations (1a)–(1b). To illustrate this, consider, for example, flow inside an impermeable-wall box. The boundary condition (4d) reduces to $\partial \bar{p}^{n+1}/\partial n = 0$; the correct boundary condition can be obtained from the semi-discrete equation (2)

$$\frac{\partial \bar{p}^{n+1}}{\partial \mathbf{n}} = \mathbf{n} \cdot \left[\sum_{q=0}^{J_e - 1} \beta_q \mathbf{N}(\mathbf{v}^{n-q}) + \nu \sum_{q=0}^{J_i - 1} \gamma_q \mathbf{L}(\mathbf{v}^{n+1-q}) \right] \qquad \text{on} \quad \partial\Omega. \tag{4e}$$

The right-hand side of this equation is not zero and is independent of the discretization parameter Δt, so that the errors induced by (4d) may be of $\mathcal{O}(1)$. However, imposition of the boundary condition (4e) involves terms at time level $(n+1)$ and leads to a coupled system.

The exact form of the pressure equation as derived in [2] is

$$\nabla^2 \bar{p}^{n+1} = \nabla \cdot \left[\left(\frac{\hat{\mathbf{v}}}{\Delta t} \right) + \nu \sum_{q=0}^{J_i - 1} \gamma_q \mathbf{L}(\mathbf{v}^{n+1-q}) \right] \qquad \text{in} \quad \Omega \tag{4f}$$

which follows from the requirement that an elliptic equation for the divergence be homogeneous (see also Section 2.3). In practice, however, Eq. (4c) is sufficiently accurate [2].

2.1. *High-Order Pressure Boundary Condition*

The obvious alternative therefore is to approximate the linear terms on the boundary via an explicit type scheme of order J_e, so that Eq. (4e) is replaced by

$$\frac{\partial \bar{p}^{n+1}}{\partial n} = \mathbf{n} \cdot \left[\sum_{q=0}^{J_e - 1} \beta_q \mathbf{N}(\mathbf{v}^{n-q}) + \nu \sum_{q=0}^{J_e - 1} \beta_q \mathbf{L}(\mathbf{v}^{n-q}) \right] \qquad \text{on} \quad \partial\Omega. \tag{5a}$$

A similar approach was suggested ini [2], where a first-order Euler-forward scheme ($J_e = 1$) was employed for the linear terms; it was shown in [2] that such a

boundary condition leads to instabilities. However, extending the ideas of [2], a stable scheme can be constructed by rewriting the viscous linear terms in terms of a solenoidal part which we approximate by an explicit scheme and an irrotational part ∇Q which is approximate by an implicit scheme of appropriate order, as

$$\frac{\partial \bar{p}^{n+1}}{\partial n} = \mathbf{n} \cdot \left[\sum_{q=0}^{J_e-1} \beta_q \mathbf{N}(\mathbf{v}^{n-q}) + \nu \sum_{q=0}^{J_i-1} \gamma_q \nabla Q^{n+1-q} + \nu \sum_{q=0}^{J_e-1} \beta_q (-\nabla \times (\nabla \times \mathbf{v})^{n-q}) \right]. \tag{5b}$$

Note that in this latter equation we drop the term $\gamma_0 \nabla Q^{n+1}$ (since we require that $Q^{n+1}=0$ in order to honor the incompressibility constraint). To demonstrate how the form (5b) of the pressure boundary condition prevents propagation and accumulation of time-differencing errors, we consider a first-order scheme ($J_e = J_i = 1$); here for simplicity we drop the non-linear terms and define $\omega_s \equiv \mathbf{n} \cdot \nabla \times (\nabla \times \mathbf{v})$. The exact equation (4e) at time level $(n+1)$ therefore reads

$$\frac{\partial \bar{p}^{n+1}}{\partial n} = \nu \left(\frac{\partial Q^{n+1}}{\partial n} - \omega_s^{n+1} \right). \tag{6a}$$

If we expand ω^{n+1} around time level n and solve for the normal derivative of the divergence we obtain

$$\frac{\partial Q^{n+1}}{\partial n} = \frac{1}{\nu} \frac{\partial \bar{p}^{n+1}}{\partial n} + \omega_s^n + \Delta t \frac{\partial \omega_s^n}{\partial t} + \cdots. \tag{6b}$$

Finally, incorporating the pressure boundary condition (5b) gives

$$\frac{\partial Q^{n+1}}{\partial n} \propto \Delta t \frac{\partial \omega_s^n}{\partial t}. \tag{6c}$$

If we instead write the viscous terms as the Laplacian operator on $\mathbf{v}$, we have

$$\frac{\partial Q^{n+1}}{\partial n} = \frac{1}{\nu} \frac{\partial \bar{p}^{n+1}}{\partial n} - \mathbf{n} \cdot \nabla^2 \mathbf{v}^n + \frac{\partial Q^n}{\partial n} + \Delta t \frac{\partial \omega_s^n}{\partial t} + \cdots \tag{6d}$$

and due to the pressure boundary condition we obtain

$$\frac{\partial Q^{n+1}}{\partial n} \propto \frac{\partial Q^n}{\partial n} + \Delta t \frac{\partial \omega_s^n}{\partial t}. \tag{6e}$$

This latter equation indicates a possible instability arising from modes corresponding to unit amplification.

2.2. *Pressure Compatibility Condition*

Solution of the Poisson equation (4c) for the pressure $\bar{p}^{n+1}$ with Neumann boundary conditions (5b) requires that a compatibility condition hold. In particular, the equations for the pressure along with the boundary condition are (here we drop the superscripts)

$$\nabla^2 \bar{p} = \nabla \cdot \left(\frac{\hat{\mathbf{v}}}{\Delta t} \right) \tag{7a}$$

$$\frac{\partial \bar{p}}{\partial n} = \sum_{q=0}^{J_e - 1} \beta_q (-\nu \omega_s + \mathbf{n} \cdot \mathbf{N})^{n-q}. \tag{7b}$$

It is required that

$$\begin{aligned} \int_\Omega \nabla^2 \bar{p} \, dv &= \int_{\partial\Omega} \frac{\partial \bar{p}}{\partial n} \, dS \\ &= \int_{\partial\Omega} \sum_{q=0}^{J_e - 1} \beta_q (-\nu \omega_s + \mathbf{n} \cdot \mathbf{N})^{n-q} \, dS \\ &= \sum_{q=0}^{J_e - 1} \beta_q \int_{\partial\Omega} (-\nu \omega_s + \mathbf{n} \cdot \mathbf{N})^{n-q} \, dS \\ &= \sum_{q=0}^{J_e - 1} \beta_q \int_\Omega \nabla \cdot (-\nu \omega_s + \mathbf{N})^{n-q} \, dv \\ &= \sum_{q=0}^{J_e - 1} \beta_q \int_\Omega \nabla \cdot (\mathbf{N})^{n-q} \, dv. \end{aligned} \tag{8}$$

The last simplification is due to the earlier definition of ω_s. The solvability condition therefore requires that

$$\sum_{q=0}^{J_e - 1} \beta_q \int_\Omega \nabla \cdot (\mathbf{N})^{n-q} \, dv = \int_\Omega \nabla \cdot \left(\frac{\hat{\mathbf{v}}}{\Delta t} \right) dv. \tag{9}$$

This equation holds by the definition of $\hat{\mathbf{v}}$ in Eq. (3a); here for simplicity we assumed zero-Dirichlet boundary conditions for the velocity $\mathbf{v}^n$.

2.3. *Divergence-Boundary Layer Analysis*

An estimate of the error incurred in the velocity field due to divergence errors can be obtained by applying a simplified boundary layer analysis for the divergence $Q \equiv Q^{n+1} = \nabla \cdot \mathbf{v}^{n+1}$. More specifically, taking the divergence of Eq. (2a) and, using the substitutions (2b)–(2d), we obtain

$$\begin{aligned} \frac{Q}{\Delta t} - \gamma_0 \nu \nabla^2 Q = \frac{Q^n}{\Delta t} &+ \nabla \cdot \left(\nu \sum_{q=1}^{J_i - 1} \gamma_q \mathbf{L}(\mathbf{v}^{n+1-q}) \right) \\ &+ \nabla \cdot \left(\sum_{q=0}^{J_i - 1} \beta_q \mathbf{N}(\mathbf{v}^{n-q}) \right) - \nabla^2 \bar{p}^{n+1}. \end{aligned} \tag{10a}$$

Since the objective is to obtain $Q=0$ at the time level $(n+1)$ we set the right-hand side to zero to obtain (4f) and the divergence equation,

$$Q-\gamma_0 \nu\, \Delta t\, \nabla^2 Q=0. \tag{10b}$$

It is clear, therefore, that there exists a (numerical) boundary layer of thickness $l=\sqrt{\gamma_0 \nu\, \Delta t}$, so that $Q=Q_w e^{-s/l}$, and thus the boundary divergence is $Q_w=-l(\partial Q/\partial n)_w$. (Here s is a general coordinate normal to the boundary.) Similar order of magnitude analysis gives $Q_w=O(\partial v/\partial n)$, and thus

$$v \propto Q_w l \propto \left(\frac{\partial Q}{\partial n}\right)_\omega \gamma_0 \nu\, \Delta t. \tag{10c}$$

This relation demonstrates that the time-differencing error of the velocity field is one order smaller in Δt than the corresponding error in the boundary divergence. This result agrees with the classical splitting scheme of first-order corresponding to the inviscid-type boundary condition (4b). In particular, the order $O(1)$ errors in $\partial Q/\partial n$ result in first-order $O(\Delta t)$ errors in the velocity field. Similarly, a first-order time treatment of the pressure boundary condition should be expected to produce second-order results in the velocity field.

The above argument clearly demonstrates that the time accuracy of the global solution is directly dependent on the boundaryh values of the divergence (i.e., $\partial Q/\partial n$) and, therefore (see Eq. (6a)), on the treatment of pressure boundary conditions.

3. Numerical Results—Part 1

In this section we employ Adams explicit and implicit schemes up to third-order to implement the formulation described in Section 2. The accuracy of the overall scheme can be characterized by the set of parameters (J_e, J_p, J_i) denoting the individual accuracy of the explicit integration (nonlinear terms), the pressure boundary condition, and the implicit integration (viscous terms), respectively.

3.1. *Stokes Channel Flow*

As a first test problem we consider a time-dependent Stokes flow problem between parallel plates which has been studied extensively before analytically and numerically [2, 10]. This problem, although linear, embodies all the essential features of the incompressible Navier–Stokes equations and serves as a model to assess the effect of the treatment of the pressure boundary condition on the overall time-accuracy of the scheme. The choice of a compatible initial conditions is very important for some numerical algorithms [10] in order to obtain a unique pressure solution; a compatible two-dimensional initial field is given by

$$u=[k\cos\lambda \sinh(ky)+\lambda\cosh k \sin(\lambda y)]\sin(kx) \tag{11a}$$

$$v=[-\cos\lambda\cosh(ky)+\cosh k\cos(\lambda y)]\cos(kx), \tag{11b}$$

where $\lambda = (-\sigma/\nu - k^2)^{1/2}$, and k is the streamwise (x-direction) wave number. We would like to point out, however, that in the method proposed here the initial inconsistency can be eliminated in one time step with the use of Eq. (4f), which is of elliptic character [2]. Here, we consider the case $\nu = 1$ and $k = 1$ which corresponds to streamwise periodicity length $L_x = 2\pi$. All eigenvalues σ for this system are real and negative so the system is stable. We consider the least negative (most unstable) symmetric mode ($\sigma = -9.317739$), which is the dominant mode resolved by the direct numerical simulation.

In the following tests the accuracy of the various schemes is examined by computing a decay-rate $\tilde{\sigma}$ which is defined as (following [10]),

$$\tilde{\sigma} = -\frac{1}{\nu T} \ln \frac{v(y=0, t+T)}{v(y=0, t)}, \tag{12}$$

where the time period T is taken to be $T = 0.3$; with the above parameters the energy of the initial field has been reduced by almost five orders of magnitude after the period T. The computational domain and the velocity field at time $T = 0.3$ are shown in Fig. 1. A very high-resolution spectral element mesh was employed to eliminate any residual spatial discretization errors. We first investigate the effect of the pressure boundary condition for constant time step $\Delta t = 0.01$; in Table I we summarize the results of several simulations corresponding to different combinations (J_p, J_i). The classical splitting scheme corresponds to $\partial p/\partial n = 0$ ($J_p = 0$) (first row); in the second and third rows results are presented for ($J_p = 1, 3$), respectively; in the second and third column the reported results correspond to Euler-backward and Crank–Nicolson integration schemes for the linear terms ($J_i = 1, 2$), respectively. It is seen that although the latter effects the accuracy of $\tilde{\sigma}$, it is actually the pressure treatment that dictates the accuracy with the smallest error (10^{-4}) to occur for the highest-order pressure boundary condition ($J_e = 3$).

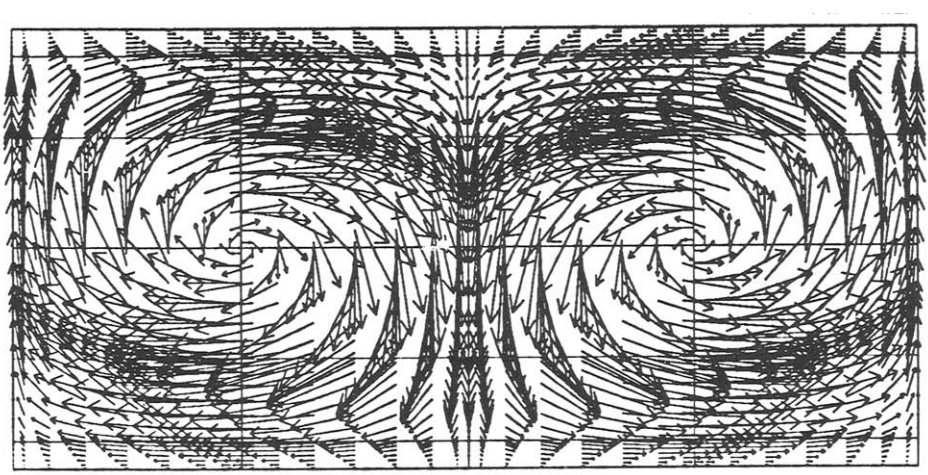

FIG. 1. Velocity vector plot of a decaying Stokes flow in a channel at time $t = 0.3$ units.

TABLE I

Effect of Pressure Boundary Condition $\Delta t = 10^{-2}$

$\partial p/\partial n$ \ Int. Order	EB	CN
$J_p = 0$	−8.78424	−9.185184
$J_p = 1$	−8.916906	−9.327403
$J_p = 3$	−8.905312	−9.314893

To examine the order of accuracy in more detail we carried out simulations for various time steps Δt for two different integration schemes: first with $(J_p = 1, J_i = 2)$ corresponding to Euler-forward for the pressure boundary condition and Crank–Nicolson for the viscous terms (EF/CN); and second with $(J_p = 3, J_i = 2)$ corresponding to third-order Adams–Bashforth, Crank–Nicholson, respectively (AB3/CN). We also obtained, for reference, results of a similar spectral element simulation that is based on the Uzawa (non-splitting) first-order scheme [14]. In Fig. 2 we plot the error in the decay-rate $\tilde{\sigma}$ versus time step Δt for these three schemes. It is seen that indeed the AB3/CN scheme obtains second-order accuracy consistent with the aforementioned analysis. It is also verified that the (EF/CN)

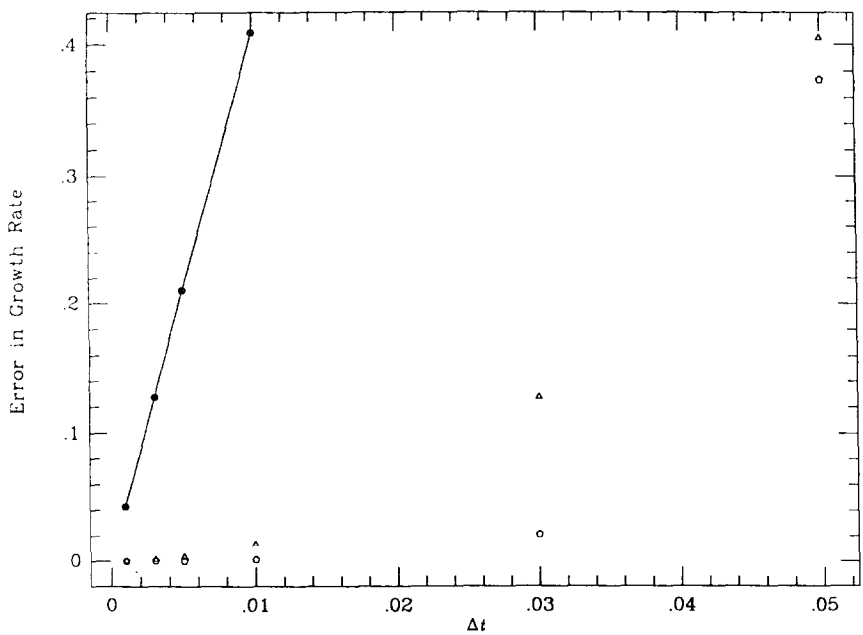

FIG. 2. Error in decay-rate versus time-step for the Stokes flow of Fig. 1: solid line, Uzawa scheme; Δ, Euler–Forward/Crank–Nicholson scheme; ◇, Adams–Bashforth 3rd/Crank–Nicholson scheme.

TABLE II

θ-Scheme Accuracy $\Delta t = 10^{-2}$

θ	0 (CN)	0.1	0.2	0.4	0.5 (EB)	Uzawa
$\tilde{\sigma}$	−9.314897	−9.229633	−9.146342	−8.984164	−8.905312	−8.905312

scheme obtains second-order accuracy; this result is also in complete agreement with the analysis reported in [2], where it was shown that a first-order pressure boundary condition of the form employing the tangential velocity (Eq. (5b)) can result in second-order overall accuracy; it is also consistent with our previously described order of magnitude analysis (Section 2.3). Finally, the zero-order pressure boundary condition leads to identical results as the Uzawa scheme, i.e., first order.

To examine the stability of the above schemes and in particular the effect of the explicit treatment of pressure boundary condition we carried out a number of tests with relatively large ($\Delta t = \mathcal{O}(1)$) time steps. After systematic experimentation we concluded that schemes that incorporate the Euler-backwards integration for the linear terms are stable irrespective of the order of the boundary condition. However, use of the Crank–Nicholson scheme may lead to instabilities for large time-steps; here, for example, this instability first appears at $\Delta t = 0.1$. Such an instability has also been realized by others [10] and is referred to as short-wave instability. To overcome this we replaced the Crank–Nicolson rule with the θ-scheme that introduces damping and is more stable [16]; indeed the resulted overall scheme eliminates the short-wave instability. However, its accuracy although of formally second-order it degrades relatively fast as $\theta \to 0.5$ (approaching the Euler-backwards limit); this is verified in Table II, where we compare the predicted decay-rate $\tilde{\sigma}$ using various values of the parameter θ.

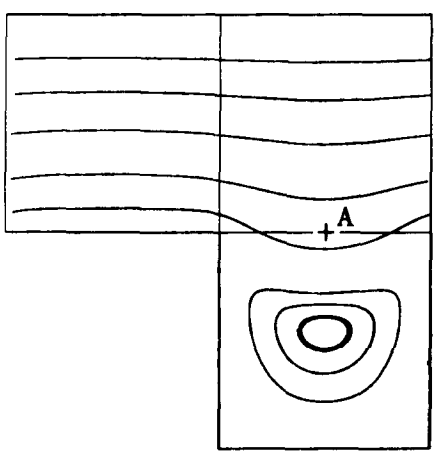

FIG. 3. Steady-state streamlines of Stokes flow in a periodic grooved channel.

3.2. *Grooved Channel Flow*

To further investigate numerically the stability of the scheme we solved an inflow/outflow Stokes problem in the grooved channel geometry (Fig. 3). The results from this experiment verified our previous conclusion, i.e., the instability present at relatively large Δt is due to the Crank–Nicholson rule and can be suppressed using a θ-scheme. This is illustrated graphically in Fig. 4, where the time-history of the streamwise velocity component at a fixed point is plotted for

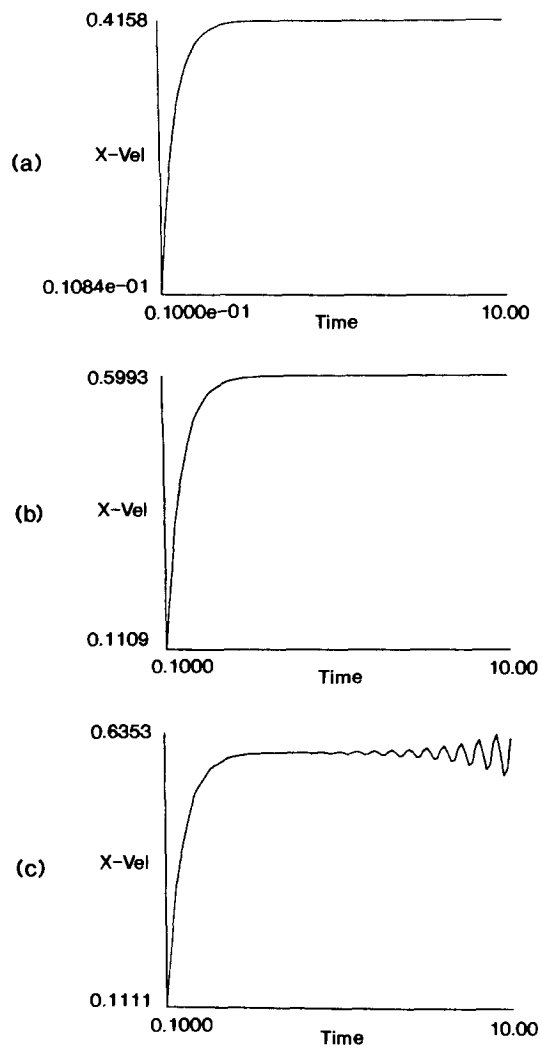

FIG. 4. Velocity versus time at point (A) (see Fig. 3) for different integration schemes: (a) $\theta = 0$, $\Delta t = 10^{-2}$; (b) $\theta = 0.1$, $\Delta t = 10^{-1}$; (c) $\theta = 0.05$, $\Delta t = 10^{-1}$.

various values of θ; it is seen that a minimum amount of damping is required to eliminate the aforementioned instability. In order to also examine the effect of the new formulation on the incompressibility of the simulated field we compute the streamwise velocity profile at the outflow using three different formulations: (A) the Uzawa formulation in which the incompressibility constraint is satisfied exactly, (B) the classical splitting scheme with zero-order pressure boundary condition, and (C)

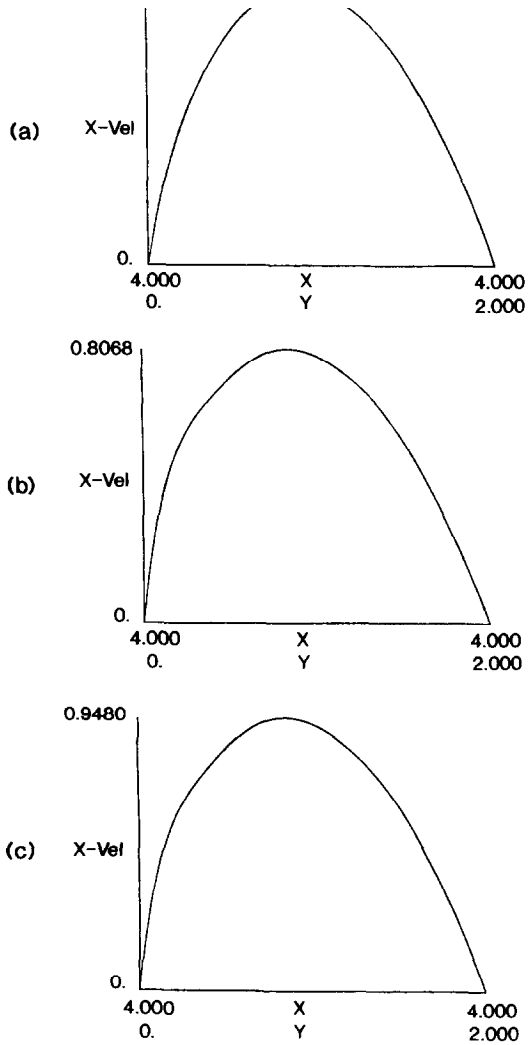

FIG. 5. Streamwise-velocity profile of the Stokes flow described in Fig. 3 computed at the exit of the domain using different time integration schemes: (a) Uzawa, (b) classical splitting, (c) splitting with improved pressure boundary condition.

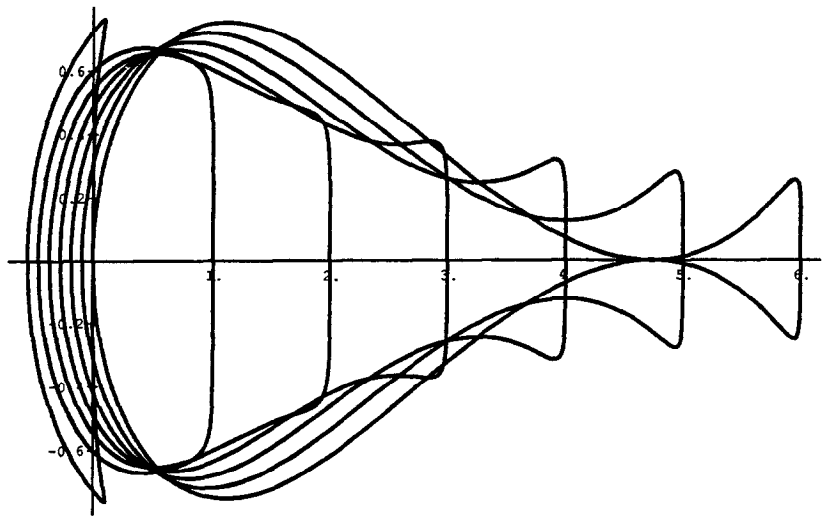

FIG. 6. Stability diagram of the mixed explicit–implicit Adams–Bashforth/Adam–Moulton of third order. The curves correspond to different values of the damping coefficient μ ($\mu = 0$ corresponds to the explicit scheme).

is established (starting from zero initial conditions) there is a significant error (15%) in the mass exiting the domain for simulation (B), whereas there is only a 0.2% error corresponding to formulation (C). A consistent formulation for outflow boundary conditions is currently underway to address the problems associated with outflow boundaries in unbounded domains.

The implementation of the above formulation to higher than second-order time-accurate schemes requires the incorporation of a higher-order integration rule for the linear terms. To achieve, for example, third-order accuracy a third-order Adams–Bashforth scheme for the pressure BC should be followed by a third-order Adams–Moulton scheme for the viscous corrections. The latter is only conditionally stable, however, with a relatively small region of stability that diminishes for higher wave numbers; this illustrated graphically in Fig. 6, where we plot the stability diagram of a mixed Adams–Bashforth/Adams–Moulton scheme. Numerical

TABLE III

Stokes Flows in a Groove with Values of U at a Fixed Point

$\partial p/\partial n$ / Δt	$J_p = 0$			$J_p = 1$			$J_p = 3$		
	EB	CN	AM3	EB	CN	AM3	EB	CN	AM3
0.005	0.4087		0.4087				0.40339		0.4073
0.01		0.4234	Unstable		0.4158	Unstable		0.4158	Unstable
0.1					0.5992	Unstable	0.5991	Unstable	Unstable

experimentation for the same range of parameters as in the previous tests verified that indeed a mixed AB3/AM3 scheme is inappropriate for all practical reasons; results are summarized in Table III. In the following section we will introduce a new class of integration schemes that can readily be used to construct arbitrarily high-order stable schemes according to the formulation of Section 2.

4. Stiffly Stable Schemes

4.1. *Stability Properties*

To extend the formulation described in Section 2 to higher-order algorithms we need to include high-order implicit schemes for the integration of the linear term. In order to avoid severe constraints A-stable methods should be used; however, according to Dahlquist [24] theorem multistep methods that are A-stable cannot have order greater than two. An alternative approach can be followed by adopting stiffly stable methods commonly used in chemical kinetic studies. According to Gear [15] a method is stiffly stable it it is accurate for all components around the origin in the stability diagram and absolutely stable away from the origin in the left imaginary plane [15]. Stiffly stable multistep methods are implicit and are available up to eleventh order [17].

Stiffly stable methods have not been studied thoroughly especially in the context of solving the Navier–Stokes equations which have both diffusive and convective contributions. As mentioned earlier, efficiency dictates a mixed explicit–implicit discretization for the convective and diffusive terms, respectively. The stability properties of such mixed schemes are best analyzed by following an approach similar to the one given by Gear [15] in studying implicit stiffly-stable schemes. Our contribution is in extending that approach to investigate the effect of an implicit viscous term on the stability properties of an explicit scheme. Geometrically the viscous contribution modifies the marginal stability curve in the stability diagram; this curve is defined here as the locus in the complex plane of all points corresponding to an amplification factor of one. The model equation for our investigation is given by

$$\frac{\partial u}{\partial t} = \mu \frac{\partial^2 u}{\partial x^2} + U \frac{\partial u}{\partial x}, \tag{13a}$$

where U is a constant convective velocity ($U = 1$) and μ is a damping constant. If we consider periodicity conditions we can obtain the modal equation (for mode k and eigenfunction u^*),

$$\frac{\partial u^*}{\partial t} = -\mu k^2 u^* + iku^*; \tag{13b}$$

for $\mu = 0$ we recover the marginal stability curve of an explicit scheme. To construct a family of curves we simply assign different values to the constant μk^2.

Following this approach we analyzed several widely used mixed schemes combining different order schemes from the Adams-family. We also developed and analyzed mixed pairs consisting of the stiffly-stable schemes for the explicit part and appropriate explicit companion schemes. For example, in Fig. 7 we plot the stability diagram of a third-order stiffly-stable mixed scheme: we see that this scheme is similar to schemes of the Adams-family, where a small amount of dissipation stabilizes the convection terms; however, with the important difference that the stability region of these combined schemes is significantly broader as seen by comparing with Fig. 6.

4.2. *Splitting Method*

Unlike the case considered in Section 2 where integration over one time step of Eq. (1a) resulted naturally in an Adams–Moulton time-stepping scheme, here we shall consider stiffly-stable type schemes in order to enhance stability. Stiffly-stable methods for ordinary differential equations are based on backwards-differentiation. For a general multistep method we approximate, for example, the time derivative in the equation

$$\frac{\partial u}{\partial t} = f \quad \text{as} \quad \frac{1}{\Delta t}\left(\gamma_0 u^{n+1} - \sum_{i=0}^{J-1} \alpha_i u^{n-i}\right), \tag{14a}$$

where for consistency we require $\gamma_0 = \sum_{i=0}^{J-1} \alpha_i$. It follows that (14a) can be rewritten as

$$\frac{1}{\Delta t} \sum_{i=0}^{J-1} \alpha_i (u^{n+1} - u^{n-i}). \tag{14b}$$

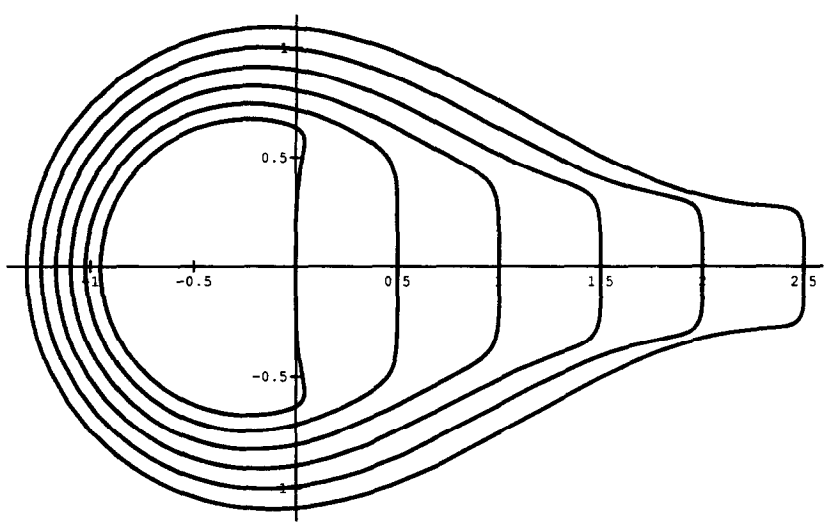

FIG. 7. Stability diagram of the mixed explicit-implicit stiffly-stable scheme of third-order ($\mu = 0$ corresponds to the explicit scheme).

We can further make use of the exact relations

$$\frac{1}{\Delta t}\sum_{i=0}^{J-1}\alpha_i(u^{n+1}-u^{n-i})=\frac{1}{\Delta t}\sum_{i=0}^{J-1}\alpha_i\int_{(n-i)\Delta t}^{(n+1)\Delta t}\frac{\partial u}{\partial t}\,dt \tag{14c}$$

$$=\frac{1}{\Delta t}\sum_{i=0}^{J-1}\alpha_i\int_{(n-i)\Delta t}^{(n+1)\Delta t} f\,dt. \tag{14d}$$

We can now split the integrand on the right-hand side f into several parts as $f=f_1+f_2+f_3$ and evaluate each part independently explicitly or implicitly. Following this approach for the Navier–Stokes equations, therefore, we obtain

$$\frac{\gamma_0\mathbf{v}^{n+1}-\sum_{q=0}^{J_i-1}\alpha_q\mathbf{v}^{n-q}}{\Delta t}=-\nabla\bar{p}^{n+1}+\sum_{q=0}^{J_e-1}\beta_q\mathbf{N}(\mathbf{v}^{n-q})+\nu\mathbf{L}(\mathbf{v}^{n+1}), \tag{15}$$

where the coefficients γ_0, α_q are the standard coefficients of (implicit) stiffly stable schemes corresponding to order J_i. The coefficients β_q for the explicit contributions are different than the ones defined in Eq. (2c) and can be readily computed by the method of undetermined coefficient and employing Taylor series expansions. In Table IV, we summarize the values of coefficients γ_0, α_q, β_q for schemes up to third-order; the first-order scheme corresponds to Euler-forward/backward integration rule.

To proceed with the splitting method we follow the three-step substeps (as in Section 2) that satisfy Eq. (15), i.e.,

$$\frac{\hat{\mathbf{v}}-\sum_{q=0}^{J_i-1}\alpha_q\mathbf{v}^{n-q}}{\Delta t}=\sum_{q=0}^{J_e-1}\beta_q\mathbf{N}(\mathbf{v}^{n-q}) \quad \text{in } \Omega \tag{16a}$$

$$\frac{\hat{\hat{\mathbf{v}}}-\hat{\mathbf{v}}}{\Delta t}=-\nabla\bar{p}^{n+1} \quad \text{in } \Omega \tag{16b}$$

$$\frac{\gamma_0\mathbf{v}^{n+1}-\hat{\hat{\mathbf{v}}}}{\Delta t}=\nu\nabla^2\mathbf{v}^{n+1} \quad \text{in } \Omega. \tag{16c}$$

TABLE IV

Stiffly-Stable Schemes Coefficients

Coefficient	1st Order	2nd Order	3rd Order
γ_0	1	3/2	11/6
α_0	1	2	3
α_1	0	−1/2	−3/2
α_2	0	0	1/3
β_0	1	2	3
β_1	0	−1	−3
β_2	0	0	1

The boundary condition for the pressure is again given by Eq. (5b), where the coefficients β_q are the modified coefficients given in Table IV.

4.3. *Normal Mode Analysis*

The methods introduced in Sections 2 and 4.1 can be analyzed for both stability and accuracy using a normal mode analysis applied to a general-geometry domain for a Stokes problem.

4.3.1. *Continuous problem.* Taking the divergence of Eq. (1a) and dropping the nonlinear terms we obtain an equation for the pressure given by

$$\nabla^2 p = 0 \tag{17a}$$

while taking the $\nabla\times\nabla\times$ of (1a) and, using the incompressibility constraint (Eq. (1b)), we obtain

$$\left(\frac{\partial}{\partial t} - \nu\nabla^2\right)\nabla^2\mathbf{v} = 0. \tag{17b}$$

To proceed we assume the existence of normal mode expansions in the form

$$\mathbf{v}(\mathbf{x}, t) = \sum_{i=1}^{\infty} e^{\sigma_i t}\mathbf{v}_i(\mathbf{x}) \tag{17c}$$

$$p(\mathbf{x}, t) = \sum_{i=1}^{\infty} e^{\sigma_i t} p_i(\mathbf{x}), \tag{17d}$$

where $\mathbf{v}_i(\mathbf{x})$ are the velocity normal modes known to have decay rates σ_i with non-positive real parts, and $p_i(\mathbf{x})$ are the pressure modes. Substituting above in Eq. (17b), we obtain the equations that the modes satisfy,

$$\nabla^2 p_i = 0 \tag{17e}$$

$$\left(\frac{\sigma_i}{\nu} - \nabla^2\right)\nabla^2\mathbf{v}_i = 0. \tag{17f}$$

It follows from the above relations that the modes $p_i(\mathbf{x})$ are harmonic and satisfy a maximum principle theorem and that the modes $\mathbf{v}_i$ have a harmonic part and an oscillatory part since $Re[\sigma_i] \leqslant 0$.

4.3.2. *Semi-discrete problem.* Using an implicit integration multistep scheme we can write the Stokes equation in a semi-discrete form as

$$\frac{\gamma_0\mathbf{v}^{n+1} - \sum_{q=0}^{J_i-1}\alpha_q\mathbf{v}^{n-q}}{\Delta t} = -\nabla\bar{p}^{n+1} + \nu\sum_{q=0}^{J_i-1}\beta_q\nabla^2(\mathbf{v}^{n+1-q}). \tag{18a}$$

Assuming for the normal modes that $(\mathbf{v}_i^n, p_i^n) = \kappa^n(\tilde{\mathbf{v}}_i, \tilde{p}_i)$, we obtain

$$\left(\frac{\gamma_0\kappa - P(\kappa)}{\Delta t}\right)\tilde{\mathbf{v}}_i = -\kappa\nabla\tilde{p}_i + \nu R(\kappa)\nabla^2\tilde{\mathbf{v}}_i, \tag{18b}$$

where we define the linear operators P, R as

$$P(\kappa)=\sum_{q=0}^{J_i-1}\alpha_q\kappa^{-q} \qquad \text{and} \qquad R(\kappa)=\sum_{q=0}^{J_i-1}\beta_q\kappa^{1-q}. \tag{18c}$$

Following a similar approach as before for the continuous problem, we now obtain

$$\nabla^2\tilde{p}_i=0 \tag{18d}$$

$$\left(\frac{\sigma_i}{\nu}-\nabla^2\right)\nabla^2\tilde{\mathbf{v}}=0 \tag{18e}$$

where $\sigma_i=\gamma_0-P(\kappa_i)/\Delta t R(\kappa_i)$. This expression is general and is valid for any multi-step method, for example, for a Crank–Nicholson scheme, $\gamma_0=1$, $P=1$, and $R=(\kappa+1)/2$, and for a second-order stiffly stable scheme, $\gamma_0=3/2$, $P=2-1/2\kappa$, and $R=\kappa$.

We find therefore by comparing with the results of the continuous case that the same modes and same σ_i are appropriate for the time discretized problem. However, negative σ_i implies that κ is less than unity for any stable time-stepping scheme.

4.3.3. *Splitting formulation.* Uncoupling of the governing equations (1) can be obtained by introducing a non-divergent intermediate velocity projection $\mathbf{v}^*$ and corresponding eigenmode $\tilde{\mathbf{v}}^*$. Again assuming a modal decomposition with amplification factor $\tilde{\kappa}$ we obtain

$$\tilde{\mathbf{v}}^*-P(\tilde{\kappa})\tilde{\mathbf{v}}=-\nabla p\tilde{\kappa}\,\Delta t \tag{19a}$$

$$\nabla\cdot\mathbf{v}^*=0 \tag{19b}$$

$$\gamma_0\tilde{\kappa}\mathbf{v}-\mathbf{v}^*=\nu\,\Delta t R(\tilde{\kappa})\nabla^2\mathbf{v}. \tag{19c}$$

Elimination of $\mathbf{v}$ followed by an operation with $\nabla\times\nabla\times$ and using (19b) gives

$$\left[\frac{\gamma_0\tilde{\kappa}-P(\tilde{\kappa})}{\nu\,\Delta t R(\tilde{\kappa})}-\nabla^2\right]\nabla^2\tilde{\mathbf{v}}^*=\left(\frac{\tilde{\sigma}}{\nu}-\nabla^2\right)\nabla^2\tilde{\mathbf{v}}^*=0, \tag{20}$$

where here we can again define a decay-rate $\tilde{\sigma}$ equal to the first term in the parenthesis above as before. The final velocity $\tilde{\mathbf{v}}$, however, satisfies a different equation obtained from (19c) of the form

$$\left(\frac{\tilde{\sigma}}{\nu}-\nabla^2\right)\nabla^2\left[\frac{\gamma_0\tilde{\kappa}}{\nu\,\Delta t R(\tilde{\kappa})}-\nabla^2\right]\mathbf{v}=0. \tag{21}$$

We see, therefore, that $\mathbf{v}^*$ satisfies an equation similar to that of the continuous problem and thus has two non-divergent modes (the pressure and the time-stepping modes corresponding to the Laplacian and time-dependent operator in Eq. (21), respectively). However, the final velocity $\tilde{\mathbf{v}}$ has an extra mode producing a numerical boundary layer of thickness $l\propto(\nu\,\Delta t)^{1/2}$ (the last operator in Eq. (21)). In the

following, we analyze the effect of this splitting error on the accuracy and stability of the overall scheme.

4.3.4. *Two-dimensional example with one periodic direction.* Here we re-examine the flow problem described in Section 3 and analyzed also in [2]. For the x-direction being periodic we can write the equation for the modes corresponding to wave number k as

$$\mathbf{v}(x, y) = (\tilde{u}(y), \tilde{v}(y))e^{ikx}. \tag{22}$$

From [2] we get the (symmetric) eigenvalue equation for a non-split formulation as

$$k \tanh k = -\mu \tan \mu, \qquad \text{where} \quad \mu^2 = -k^2 - \sigma/\nu. \tag{23}$$

For the current problem the general operators appearing in (4a)–(4c) can be rewritten as

$$\nabla^2 = D^2 - k^2, \qquad \nabla^2 - \frac{\tilde{\sigma}}{\nu} = D^2 + \tilde{\mu}^2, \qquad \nabla^2 - \frac{\gamma_0 \tilde{\kappa}}{\nu\, \Delta t \tilde{R}} = D^2 - \lambda^2, \tag{24a}$$

where we have used the definitions

$$\tilde{\mu}^2 = -k^2 - \frac{\tilde{\sigma}}{\nu}, \qquad \lambda^2 = k^2 + \frac{\gamma_0 \tilde{\kappa}}{\nu\, \Delta t \tilde{R}} \tag{24b}$$

$$\tilde{P} = P(\tilde{\kappa}), \qquad \tilde{R} = R(\tilde{\kappa}) \tag{24c}$$

$$D = \frac{d}{dy}. \tag{24d}$$

The general form of the solution $\tilde{v}$, $\tilde{v}^*$ that is symmetric about $y = 0$ is

$$\tilde{v}^* = \gamma_0 A^* \cosh ky + \gamma_0 B^* \cos \tilde{\mu} y \tag{25a}$$

$$\tilde{v} = \tilde{A} \cosh ky + \tilde{B} \cos \tilde{\mu} y + \tilde{C} \cosh \lambda y. \tag{25b}$$

We now consider each of the modes (k, μ, λ) separately; the first two are non-divergent as was mentioned earlier. Considering, for example, first the mode k as

$$\tilde{v}_k^* = \gamma_0 A^* \cosh ky, \qquad \tilde{v}_k = \tilde{A} \cosh ky \tag{26a}$$

and substituting in (19c), we obtain

$$\tilde{A} = A^*/\tilde{\kappa}. \tag{26b}$$

The corresponding velocity in the x-direction is obtained from the divergence-free condition

$$\tilde{u}_k = -\frac{D\tilde{v}_k}{ik} = i \sinh ky \frac{A^*}{\tilde{\kappa}}. \tag{26c}$$

Similarly, for the second mode we obtain the relations

$$\tilde{B} = \frac{\gamma_0 B^*}{\tilde{P}} \qquad \text{and} \qquad \tilde{u}_\mu = -\frac{i\tilde{\mu}}{k}\tilde{B}\sin\tilde{\mu}y. \tag{27}$$

Finally, for the non-divergent third mode for which $v_\lambda^* = 0$, we obtain again from (4a)

$$-\tilde{P}\mathbf{v}_\lambda = -\tilde{\kappa}\,\nabla p\,\Delta t \tag{28a}$$

and therefore the field $\mathbf{v}_\lambda$ is irrotational, i.e., $\nabla \times \mathbf{v}_\lambda = 0$; this implies that the following relation holds:

$$D\tilde{u}_\lambda = ik\tilde{v}_\lambda. \tag{28b}$$

To summarize, we can now express the modes $(\tilde{u}, \tilde{v})$ as (setting $\tilde{C} = C^*$)

$$\tilde{v} = \frac{A^*}{\tilde{\kappa}}\cosh ky + \frac{\gamma_0 B^*}{\tilde{P}}\cos\tilde{\mu}y + C^*\cosh\lambda y \tag{29a}$$

$$\tilde{u} = \frac{iA^*}{\tilde{\kappa}}\sinh ky - \frac{i\gamma_0\tilde{\mu}B^*}{k\tilde{P}}\sin\tilde{\mu}y + iC^*\frac{k}{\lambda}\sinh\lambda y. \tag{29b}$$

At this point we can find C^* in terms of A^* by employing the boundary condition at $y = 1$ $(\tilde{u} = \tilde{v} = 0)$, i.e.,

$$C^* = -\frac{A^*\cosh k(\tilde{\mu}\tan\tilde{\mu} + k\tanh k)}{\tilde{\kappa}\cosh\lambda(\tilde{\mu}\tan\tilde{\mu} + (k^2/\lambda)\tanh\lambda)}. \tag{30}$$

Using the exact eigenvalue relation (Eq. (23)) and the definition equation (24b), we also obtain

$$\tilde{\mu}\tan\tilde{\mu} - \mu\tan\mu = \mathcal{O}(\Delta\sigma/\nu), \tag{31}$$

where we define $\Delta\sigma = \tilde{\sigma} - \sigma$. Substituting this last equation in (30) and normalizing appropriately with $\cosh\lambda$ we see that the amplitude C^* of the boundary layer error term is proportional to $\Delta\sigma/\nu$, i.e.,

$$C^* \propto \Delta\sigma/\nu. \tag{32}$$

This last equation suggests that the error in growth rate which characterizes the time-accuracy of the scheme is directly proportional to the amplitude of the divergent mode.

The boundary condition for the pressure can be found from (19) applied at the boundary. This is an exact equation and has the form

$$\tilde{\kappa}\,\nabla p = \nu R(\tilde{\kappa})\,\nabla^2\mathbf{v}, \tag{33}$$

where we assumed here that $\mathbf{v}=0$ at the boundary. However, this relation results in a coupled system since $\nabla^2\mathbf{v}^{n+1}$ is not known at the pressure step, so that an explicit treatment should be sought. For example, two first-order relations that can be used are

$$\tilde{\kappa}\,\nabla p = \nu\,\nabla^2\tilde{\mathbf{v}} \tag{34a}$$

$$\tilde{\kappa}\,\nabla p = -\nu\,\nabla\times\nabla\times\tilde{\mathbf{v}}, \tag{34b}$$

where in the latter equation we also incorporated the incompressibility constraint, i.e., $\nabla\cdot\mathbf{v}=0$. It follows therefore from (19a) with $\mathbf{v}(y=1)=0$ that

$$v^* + \nu\,\Delta t\,D^2\tilde{v}=0 \tag{35a}$$

$$v^* - i\nu k\,\Delta t\,D\tilde{u}=0. \tag{35b}$$

Substitution of v^*, $\tilde{u}$, $\tilde{v}$ in (35a)–(35b) gives

$$A^*\left(\gamma_0+\frac{\nu\,\Delta t k^2}{k}\right)\cosh k + B^*\gamma_0\left(1-\frac{\nu\,\Delta t\tilde{\mu}^2}{\tilde{P}}\right)\cos\tilde{\mu} + C^*\nu\lambda^2\,\Delta t\cosh\lambda = 0 \tag{36a}$$

$$A^*\left(\gamma_0+\frac{\nu\,\Delta t k^2}{\kappa}\right)\cosh k + B^*\gamma_0\left(1-\frac{\nu\,\Delta t\tilde{\mu}^2}{\tilde{P}}\right)\cos\tilde{\mu} + C^*\nu k^2\,\Delta t\cosh\lambda = 0, \tag{36b}$$

coupled with the boundary conditions $\tilde{u}=\tilde{v}=0$; to satisfy the boundary conditions and after substitution from (35a) the following determinant vanishes:

$$\begin{vmatrix} \gamma_0\tilde{\kappa}+\nu\,\Delta t^2k^2 & \tilde{P}-\tilde{\mu}^2\nu\,\Delta t & \lambda^2\nu\,\Delta t \\ 1 & 1 & 1 \\ k\tanh k & -\tilde{\mu}\tan\tilde{\mu} & k^2\dfrac{\tanh\lambda}{\lambda} \end{vmatrix} = 0. \tag{37}$$

The determinant for the case (35b) has a similar form with the term $\lambda^2\nu\,\Delta t$ above replaced by the term $k^2\nu\,\Delta t$.

We solve the above determinantal equation for the particular case of a second-order stiffly-stable scheme. The eigenvalue $\tilde{\kappa}$ corresponding to (37) agrees with the analytical expansion for κ of the non-split scheme up to first-order terms, which implies a reduction of the accuracy order of the overall scheme to order one, despite the second-order time-stepping scheme employed. However, the eigenvalue due to (35b) agrees with that of κ to second order as also found by our boundary layer analysis. The expansion for the amplification factor $\tilde{\kappa}$ of the splitting scheme is

$$\tilde{\kappa} = \kappa + \Delta\kappa \tag{38a}$$

$$= (1+\sigma\,\Delta t+\sigma^2\,\Delta t^2/2+\sigma^3\,\Delta t^3/3+\mathcal{O}(\Delta t^4)) \tag{38b}$$

$$+(\kappa_1\,\Delta t^2+\kappa_2\,\Delta t^{5/2}+\kappa_3\,\Delta t^3+\kappa_4\,\Delta t^{7/2}+\mathcal{O}(\Delta t^4)), \tag{38c}$$

where we find that $\kappa_1 = \kappa_2 = 0$ and that the next two coefficients κ_3, κ_4 are given by

$$\kappa_3 = \frac{4\tilde{\mu}^2 \nu \sigma^2 \sin 2\tilde{\mu}}{\sigma + 3 \sin 2\tilde{\mu}} \tag{39a}$$

$$\kappa_4 = \frac{8\sqrt{2}}{3\sqrt{3}} \frac{\tilde{\mu} \nu^{3/2} k^2 \sigma^2 \cos^2 \tilde{\mu}}{2\tilde{\mu} + \sin 2\tilde{\mu}}. \tag{39b}$$

We alsonote that $\Delta\sigma$ which determines the boundary layer amplitude is given by

$$\Delta\sigma = \kappa_3 \Delta t^2 + \kappa_4 \Delta t^{5/2} + \mathcal{O}(\Delta t^3). \tag{40}$$

It is seen therefore that the decay-rate $\tilde{\sigma}$ computed using the stiffly-stable splitting scheme is accurate to second order in Δt if the rotational boundary condition (Eq. (5b)) is employed for the pressure. We also see using (32)–(40) that the error in the numerical boundary layer is of second order.

5. Numerical Results—Part 2

5.1. *Stokes Channel Flow*

In this section we investigate numerically the stability and accuracy properties of the schemes described in Section 4. As a first test we consider the Stokes flow

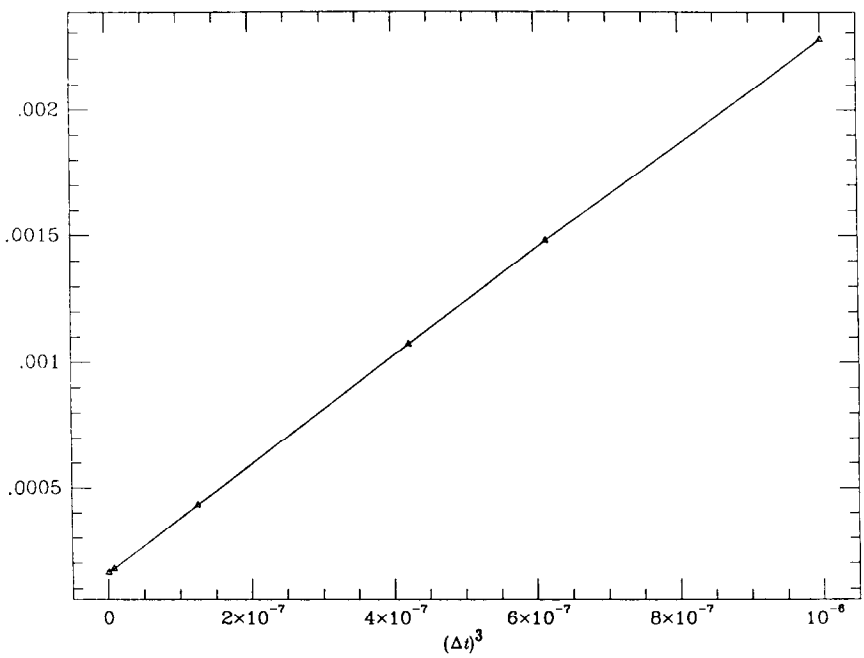

FIG. 8. Error in decay-rate versus $(\Delta t)^3$ for the Stokes flow described in Fig. 1.

problem in a smooth channel which also examined in Section 3. Here, we demonstrate that the new schemes are not only stable but they also retain their formal accuracy. To this end, we carry out simulations for several values of the time step Δt for the third-order scheme ($J_i = 3$, $J_p = 3$) and compute the decay-rate $\tilde{\sigma}$. The set of parameters as well as the initial field remains the same as in Section 4. The results of these simulations are plotted in Fig. 8 as a function of Δt^3; the straight line proves that the formal third-order accuracy of the scheme is indeed retained. In Fig. 9 we also plot the divergence across the channel at a fixed position x for the two types of the pressure BC; we see that the rotational form almost completely eliminates any residual divergence errors. A detailed study on the efficient removal of boundary-divergence errors is given elsewhere [18].

5.2. *Wannier Flow*

As a second test problem we consider a two-dimensional Stokes flow past a circular cylinder placed next to a moving wall. The available exact solution due to Wannier [19] for this complex-geometry flow allows for reliable evaluation of the time-differencing error. This problem and its variants have been recently used for

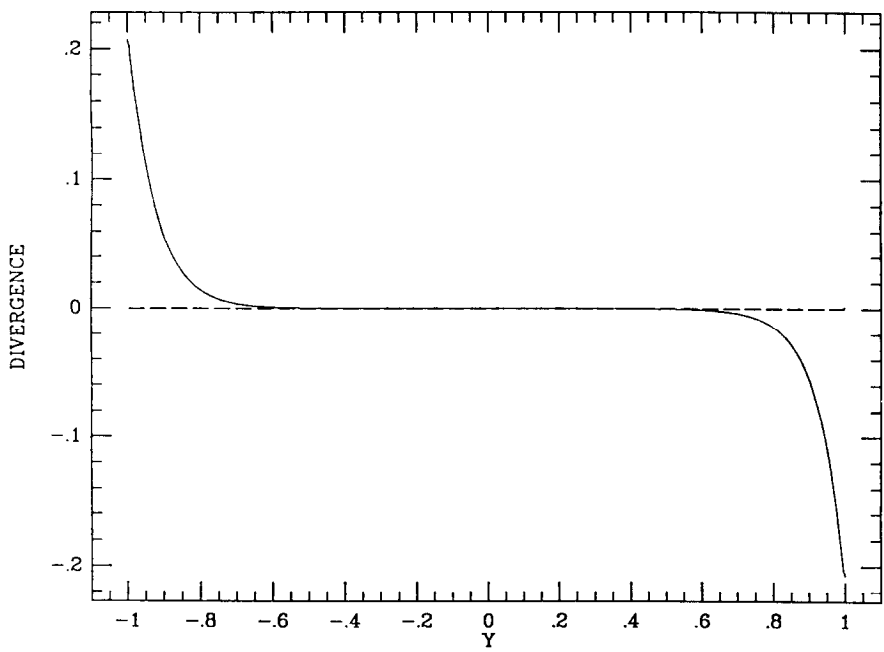

FIG. 9. Profile of divergence of the velocity field of the Stokes flow of Fig. 1 for two different types of pressure boundary conditions: solid line, $\partial p/\partial n = \nu \sum_{q=0}^{2} \beta_q \nabla^2 V^{n-q} \cdot \hat{n}$; dashed line, $\partial p/\partial n = -\nu \sum_{q=0}^{2} \beta_q \nabla \times \omega \cdot \hat{n}$.

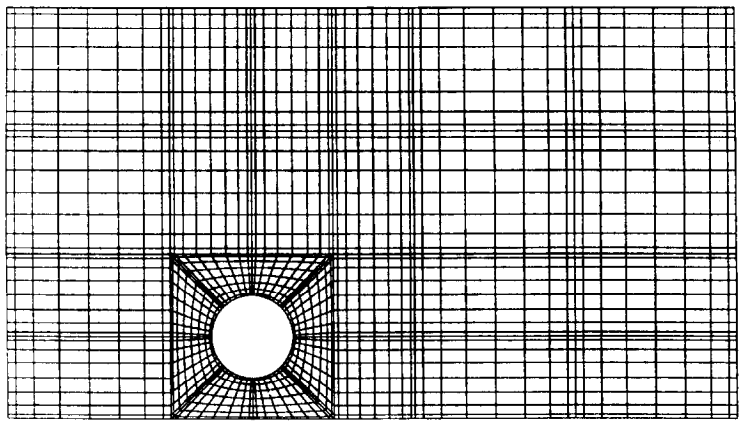

FIG. 10. Spectral element mesh for the Wannier–Stokes flow ($K=28$; $N=9$).

code verification purposes [20–22]. The exact solution and the particular parameters we use in the present test are given by

$$u=-\frac{2(A+Fy)}{K_1}\left[(s+y)+\frac{K_1}{K_2}(s-y)\right]$$
$$-F\ln\left(\frac{K_1}{K_2}\right)-\frac{B}{K_1}\left[(s+2y)-\frac{2y(s+y)^2}{K_2}\right]-D \tag{41a}$$

$$v=\frac{2x}{K_1K_2}(A+Fy)(K_2-K_1)-\frac{2Bxy(s+y)}{K_1^2}-\frac{2Cxy(s-y)}{K_2^2}, \tag{41b}$$

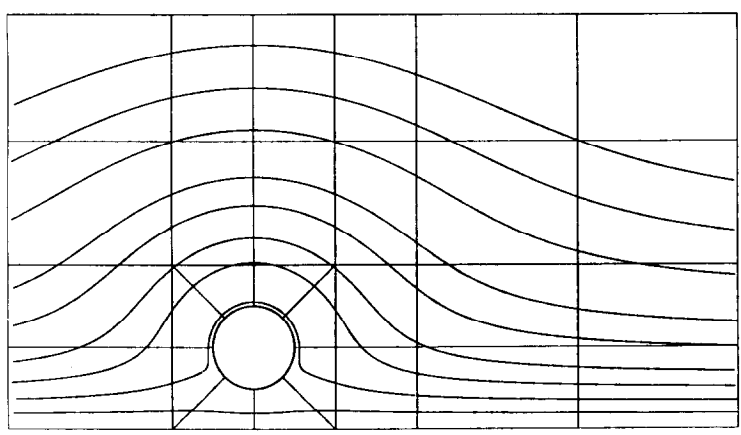

FIG. 11. Steady-state streamline pattern of the Wannier–Stokes flow.

where we define

$$A = -\frac{Ud}{\ln(\Gamma)}, \qquad B = \frac{2(d+s)U}{\ln(\Gamma)}, \qquad C = \frac{2(d-s)U}{\ln(\Gamma)}, \qquad D = -U, \qquad F = \frac{U}{\ln(\Gamma)} \tag{42a}$$

$$K_1 = x^2 + (s+y)^2, \qquad K_2 = x^2 + (s-y)^2, \qquad s^2 = d^2 - R^2, \qquad \Gamma = \frac{d+s}{d-s}. \tag{42b}$$

Here, we denote by $R = 0.25$ the cylinder radius, by $d = 0.5$ the distance of the cylinder center from the wall, and by $U = 1$ the velocity of the moving wall. The mesh employed for this simulation is shown in Fig. 10. Dirichlet BC were used at the boundaries of the truncated domain computed from the exact solution. The computed steady-state solution is shown in Fig. 11 in the form of streamline patterns, and is indistinguishable from the exact solution. In Fig. 12 we plot the convergence history to the final steady state presented as the L_2-error at $\Delta t = 10^{-2}$ versus time for four different schemes: (1) the classical splitting scheme (Eq. (3)) using the inviscid-type boundary condition (4b); and the new stiffly stable schemes corresponding to (A) first-order, (B) second-order, and (C) third-order,

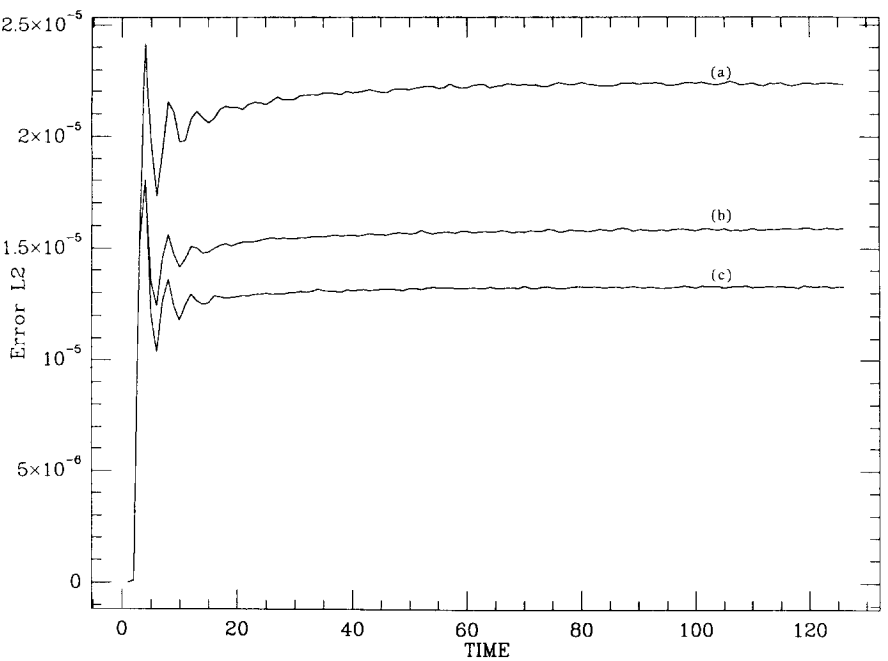

FIG. 12. Error (L_2) versus time for the Navier–Stokes flow. The different curves correspond to (a) first-order stiffly-stable scheme, (b) second-order stiffly-stable scheme, (c) third-order stiffly-stable scheme. The corresponding error using the classical splitting scheme is three orders of magnitude larger.

respectively. The superiority of the new pressure boundary condition is reflected in the difference between errors induced by (1) and curve (A), whereas the high-order time-accuracy gain is realized by comparing the curves (A), (B), and (C). The formal accuracy of the method is tested in Fig. 13, where the L_2-error is plotted as a function of Δt^2 for the second-order scheme ($J_i = 2$; $J_e = 2$); the straight line is indicative of second-order convergence.

5.3. *Kovasznay Flow*

Finally, we test the stiffly-stable schemes in the context of Navier–Stokes computations. To this end, we consider the laminar flow behind a two-dimensional grid, the exact solution of which was given by Kovasnay [23]. The solution is given as a function of the Reynolds number R in the form

$$u = 1 - e^{\lambda x}\cos(2\pi y) \tag{43a}$$

$$v = \frac{1}{2\pi} e^{\lambda x}\sin(2\pi y), \tag{43b}$$

where $\lambda = R^2/2 - (R^2/4 + 4\pi^2)^{1/2}$. The inflow/outflow boundary conditions are also defined by the above relations. The computed steady state streamline pattern is

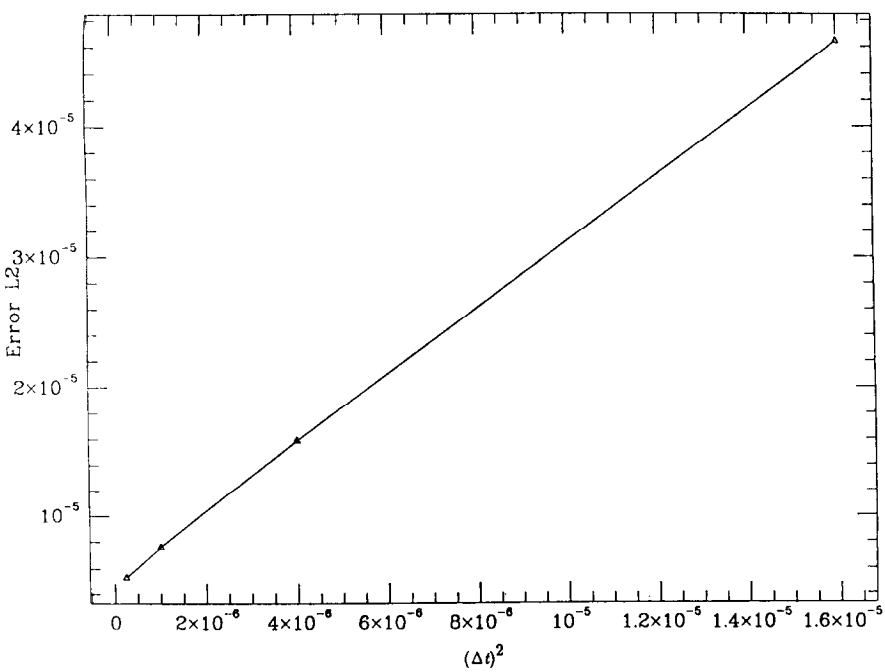

FIG. 13. Plot of error (L_2) versus $(\Delta t)^2$ demonstrating the second-order time-accuracy of a second-order stiffly-stable scheme.

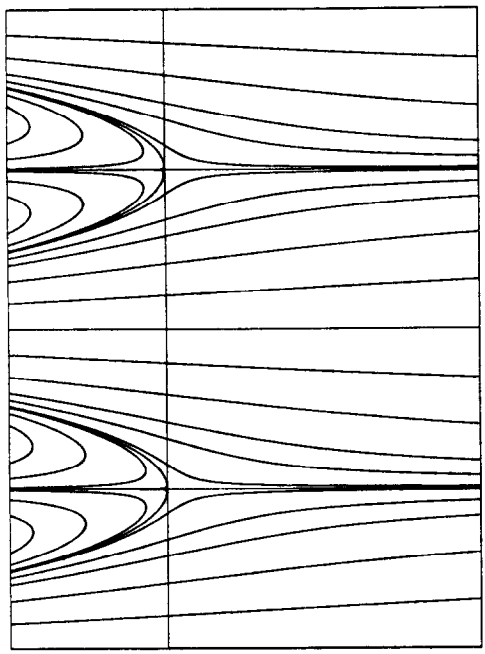

FIG. 14. Steady-state streamline patterns for the Kovasznay flow at Reynolds number $R = 40$.

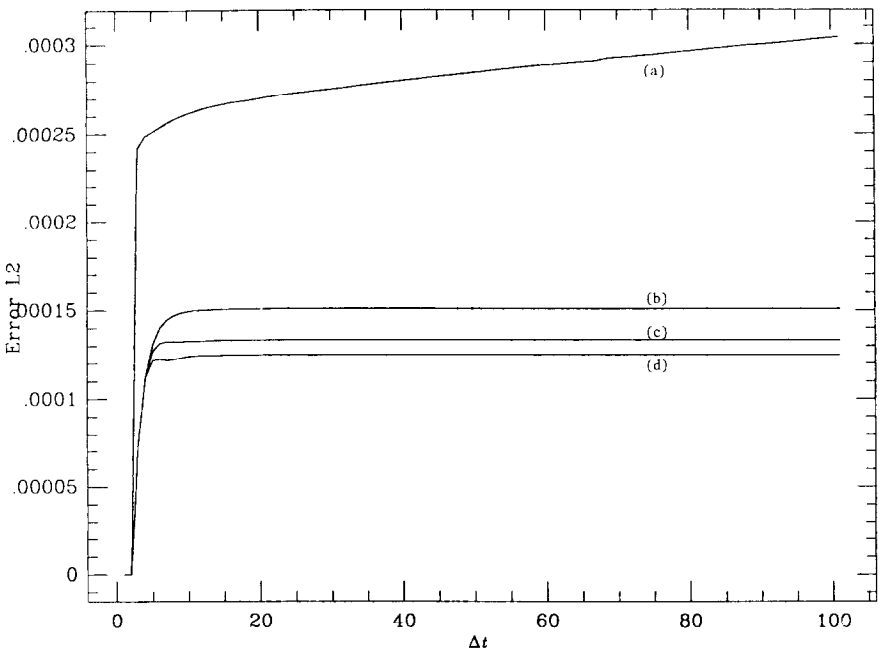

FIG. 15. Error (L_2) versus time for the Kovasznay flow: (a) classical splitting; (b) first-order mixed stiffly-stable; (c) second-order mixed stiffly-stable; (d) third-order mixed stiffly-stable scheme.

TABLE V

$\Delta t = 3.072 \times 10^{-3}$

Error \ Scheme	$J_p = 0$[a]	$J_p = 1$	$J_p = 3$		
	AB3–CN[b]	AB3–CN	SS1[c]	SS2	SS3
e_2	1.465×10^{-3}	3.463×10^{-4}	3.427×10^{-4}	2.858×10^{-4}	2.58×10^{-4}
e_∞	2.118×10^{-3}	4.779×10^{-4}	4.776×10^{-4}	4.139×10^{-4}	3.795×10^{-4}

[a] J_p denotes the integration order for pressure BC.
[b] AB3 ≡ Adams–Bashforth of third order; CN ≡ Crank–Nicholson.
[c] SS1 ≡ Stiffly-stable scheme of first order.

plotted in Fig. 14 at $R = 40$. A pair of bound eddies occur just downstream of the inflow, whereas the streamlines become parallel and equidistant at infinity. The computed solution is indistinguishable from the exact solution of Kovasznay [23].

In Fig. 15 we plot the L_2 error of the solution versus time for different orders of integration and compare the stiffly-stable schemes with the classical splitting scheme (curve A). We see again that a large error is incurred due to inviscid-type boundary condition (Eq. (4b)) and that the order of accuracy is increased with the order of integration. To compare in more detail the stability and accuracy properties of the schemes presented in Sections 2 and 4 we carried out numerical simulations at a fixed time step $\Delta t = 3.072 \times 10^{-3}$. The results are summarized in Table V for the various cases in terms of the maximum pointwise error (L_∞ norm), as well as in terms of the weighted-average error (L_2 norm). There is almost an order of magnitude decrease in both errors when the improved boundary condition is employed compared to the inviscid-type boundary condition (4b). It is also seen that the stiffly-stable schemes are superior regarding *accuracy* to the schemes based on the Adams-family integration rules. Regarding *stability*, the new schemes are also more stable than any mixed schemes of the Adams-family in agreement with the stability diagrams (Figs. 6–7) corresponding to the linear problem. Numerical experimentation indicates that for the current problem there is at least an order of magnitude gain in stability in comparing the second-order schemes, while the stability of the third-order stiffly-stable scheme is dictated by the explicit part and an approximate CFL value of one; the corresponding third-order Adams–Bansforth/Adams–Moulton (AB3/AM3) scheme is unstable for all values of time-step Δt.

ACKNOWLEDGMENTS

We acknowledge the contribution of A. Tomboulides in implementing some of the computer codes for this work. Financial support for the current work was provided by grants from NSF (CTS-8906911 and CTS-8906432), DARPA Contract N00014-86-K-0759, and ONR Contracts N00014-82-C-0451 and N0014-90-1315. One of us (M.I.) acknowledges the support of the Fund for Promotion of Research at the Technion.

REFERENCES

1. P. GRESHO AND R. SANI, On pressure boundary conditions for the incompressible Navier–Stokes equations, *Int. J. Numer. Methods Fluids* **7**, 1111 (1987).
2. S. A. ORSZAG, M. ISRAELI, AND M. O. DEVILLE, Boundary conditions for incompressible flows, *J. Sci. Comput.* **1** No. 1, 75 (1986).
3. N. YANENKO, *The Method of Fractional Steps* (Springer-Verlag, Berlin/New York, 1971).
4. S. A. ORSZAG AND L. C. KELLS, Transition to turbulence in plane Poiseuille flow and plane Couette flow, *J. Fluid Mech.* **96**, 159 (1980).
5. G. E. KARNIADAKIS, B. B. MIKIC, AND A. T. PATERA, Minimum dissipation transport enhancement by flow destabilization; Reynolds' analogy revisited, *J. Fluid Mech.* **192**, 365 (1988).
6. G. E. KARNIADAKIS AND G. S. TRIANTAFYLLOU. Frequency selection and asymptotic states of laminar wakes, *J. Fluid Mech.* **199**, 441 (1989).
7. P. S. MARCUS, Simulation of Taylor–Couette flow. Part 1. Numerical methods and comparison with experiment, *J. Fluid Mech.* **146**, 45 (1984).
8. J. KIM AND P. MOIN, Application of a fractional-step method to incompressible Navier-Stokes equation, *J. Comput. Phys.* **59**, 308 (1985).
9. T. A. ZANG AND M. Y. HUSSAINI, On spectral multigrid methods for the time-dependent Navier–Stokes equations, *Appl. Numer. Math.* **19**, 359 (1986).
10. M. O. DEVILLE, L. KLEISER, AND F. MONTIGNY-RANNOU, Pressure and time treatment for Chebyshev spectral solution of a Stokes problem, *Int. J. Numer. Methods Fluids* **4**, 1149 (1984).
11. A. T. PATERA, A spectral element method for fluid dynamics; Laminar flow in a channel expansion, *J. Comput. Phys.* **54**, 468 (1984).
12. G. E. KARNIADAKIS, E. T. BULLISTER, AND A. T. PATERA, A spectral element method for solution of two- and three-dimensional time dependent Navier–Stokes equations, *Finite Element Methods for Nonlinear Problems* (Springer-Verlag, New York/Berlin, 1985), p. 803.
13. G. E. KARNIADAKIS, Spectral element simulations of laminar and turbulent flows in complex geometries, *Appl. Numer. Math.* **6**, 85 (1989).
14. E. M. RØNQUIST, *Optimal Spectral Element Methods for the Unsteady Three-Dimensional Incompressible Navier–Stokes Equations*, Ph.D. thesis, Massachusetts Institute of Technology, 1988 (unpublished).
15. C. W. GEAR, *Numerical Initial Value Problems in Ordinary Differential Equations* (Prentice–Hall, Englewood Cliffs, NJ, 1973).
16. C. CANUTO, M. HUSSAINI, A. QUARTERONI, AND T. ZANG, *Spectral Methods in Fluid Dynamics* (Springer-Verlag, New York/Berlin, 1987).
17. M. K. JAIN AND V. K. SRIVASTAVA, *High Order Stiffly Stable Methods for Ordinary Differential Equations*, Technical Report 394, University of Illinois, Urbana, II, 1970 (unpublished).
18. A. TOMBOULIDES, M. ISRAELI, AND G. E. KARNIADAKIS, "Efficient Removal of Boundary-Divergence Errors in Time-Splitting Methods," *J. Sci. Comput.* **4**, 291 (1989).
19. G. H. WANNIER, A contribution to the hydrodynamics of lubrication, *Q. Appl. Math.* **8**, 1 (1950).
20. A. N. BERIS, R. C. ARMSTRONG, AND R. A. BROWN, Finite element calculation of viscoelastic flow in a journal bearing: Small eccentricities, *J. Non-Newtonian Fluid Mech.* **16**, 141 (1984).
21. K. Z. KORCZAK AND A. T. PATERA, An isoparametric spectral element method for solution of the Navier–Stokes equations in complex geometry, *J. Comput. Phys.* **62**, 361 (1986).
22. M. M. MASLANIK, R. L. SANI, AND P. M. GRESHO, An isoaparametric finite element Stokes flow test problem, preprint, 1989 (unpublished).
23. L. I. G. KOVASZNAY, Laminar flow behind a two-dimensional grid, *Proc. Cambridge Philos. Soc.*, p. 44 (1948).
24. DAHLQUIST, 1963.